

Atomistic simulations of grain boundary segregation in nanocrystalline yttria-stabilized zirconia and gadolinia-doped ceria solid oxide electrolytes

Hark B. Lee^{*}, Friedrich B. Prinz¹, Wei Cai²

Department of Mechanical Engineering, Stanford University, CA 94305-4040, United States

Received 27 November 2012; received in revised form 12 March 2013; accepted 14 March 2013

Available online 12 April 2013

Abstract

Hybrid Monte Carlo–molecular dynamics simulations are carried out to study defect distributions near $\Sigma 5(3\bar{1}0)/[001]$ pure tilt grain boundaries (GBs) in nanocrystalline yttria-stabilized zirconia and gadolinia-doped ceria. The simulations predict equilibrium distributions of dopant cations and oxygen vacancies in the vicinity of the GBs where both materials display considerable amounts of dopant segregation. The predictions are in qualitative agreement with various experimental observations. Further analyses show that the degree of dopant segregation increases with the doping level and applied pressure in both materials. The equilibrium segregation profiles are also strongly influenced by the microscopic structure of the GBs. The high concentration of oxygen vacancies at the GB interface due to lower vacancy formation energies triggers the dopant segregation, and the final segregation profiles are largely determined by the dopant–vacancy interaction.

© 2013 Acta Materialia Inc. Published by Elsevier Ltd. All rights reserved.

Keywords: Segregation; Grain boundary; Monte Carlo; Molecular dynamics; Nanocrystalline

1. Introduction

Yttria-stabilized zirconia (YSZ) and gadolinia-doped ceria (GDC) are widely used electrolyte materials for solid oxide fuel cells due to their high ionic conductivities. Grain boundaries (GBs) have been shown to play a significant role in the charge transport and surface kinetics of YSZ and GDC. Many experimental studies on polycrystals have reported degradation of ionic conductivity, whereas the observations on nanocrystalline YSZ and GDC are mixed. While reduced ionic conductivity is reported in some studies [1–4], the opposite is revealed in others [5–10]. Among these, nanocrystalline thin film structures fabricated by

atomic layer deposition [11] have shown significantly improved electrolyte performances over single crystals [12,13]. Most of the improvements are attributed to reduced activation loss at the cathode, which implies the potential effects of GBs on the surface kinetics of solid oxide electrolytes.

The uncertain role of GBs in electrolyte performance indicates the existence of many fundamental questions that still remain unanswered. An outstanding question is the nature of defect segregation at GBs, which affects both ionic conductivity and surface kinetics by altering the local electrostatic potential. Dopant cations have been experimentally observed to segregate at GBs [14–27] in both YSZ and GDC, but existing techniques are limited in their spatial resolutions (on the order of a few nanometers), which makes it challenging to uncover the details on the atomic scale. Furthermore, it is still impossible to directly measure the distribution of oxygen vacancies, which are the main charge carriers and are of great importance.

* Corresponding author. Tel.: +1 650 575 7150.

E-mail addresses: harkblee@gmail.com (H.B. Lee), fprinz@stanford.edu (F.B. Prinz), cawei@stanford.edu (W. Cai).

¹ Tel.: +650 723 4023; fax: +650 725 4862.

² Tel.: +650 736 1671; fax: +650 723 1778.

The space-charge theory has predicted dopant and oxygen vacancy density distributions near GBs in YSZ [28–34]. However, its applicability becomes uncertain when the defect distributions it predicts fluctuate rapidly on the atomic scale. Furthermore, the mean-field approximation in these studies does not account for the correlation between individual defects.

Atomistic simulations have been used to explain the ionic conduction or defect ordering in both YSZ and GDC [35–55]. Computational studies on the defect segregation ionic oxides have been scarce and limited in various aspects, mostly due to the limited time and length scales, and the lack of an efficient sampling algorithm to equilibrate the microstructure. Mao et al. [56] investigated the microstructure of $\Sigma 5(310)/[001]$ GB in YSZ using first-principles calculations and concluded that interfacial segregation would be energetically favorable. Oyama et al. [57] and Yoshiya et al. [58] conducted a series of atomistic simulations to investigate the GB segregation in YSZ and concluded that the elastic strain is the main driving force for the co-segregation of dopants and vacancies. While providing qualitative insights, these studies are still substantially limited in their time and length scales, and inspire the development of a more advanced and efficient simulation algorithm, through which a better understanding of the phenomenon may be attainable.

Recently, we developed a hybrid Monte Carlo (MC)–molecular dynamics (MD) algorithm [59] that successfully predicted large-scale segregation profiles of point defects at the (100) surfaces of YSZ and GDC, based on empirical interatomic potential models. In this study, we apply this method to the $\Sigma 5(310)/[001]$ GBs in YSZ and GDC to predict the near-GB equilibrium distributions of point defects.

This paper is organized as follows. Section 2 describes how to create the atomistic model of the GBs. Section 3 presents the simulation results on the distribution of point defects and how they are influenced by doping level and applied pressure. Section 4 discusses the main driving forces for dopant segregation. A brief summary is given in Section 5.

2. Methods

2.1. Interatomic potentials and simulation algorithm

The interatomic potential models and simulation methods in this study are identical to those in our previous work [59]. YSZ and GDC are assumed to be fully ionic, and the interactions between ions are modeled by the combination of a short-range Born–Mayer–Buckingham (BMB) potential and long-range Coulomb potential [51,60,61]. The functional form of the interatomic potentials and the parameters are presented in Appendix A. An implicit assumption is made that these potentials are valid for the GB interface, although they are empirically fitted to the properties of the bulk.

After the atomic structures are constructed (Section 2.2), they are equilibrated using the hybrid MC–MD algorithm [59]. The MC part of the algorithm alters the cation distributions, and the MD part is mainly responsible for the redistribution of oxygen vacancies as well as the collective equilibration of all ions. The MC trial move is designed to switch the positions of a randomly chosen pair of dopant (Y^{3+} in YSZ and Gd^{3+} in GDC) and host (Zr^{4+} in YSZ and Ce^{4+} in GDC) cations. The MC move is accepted or rejected according to the potential energy difference it introduces, based on the Metropolis algorithm [62]. To overcome the limited time scale of atomistic simulations, neighboring ions of the switching cation pair are also displaced according to a pair of pre-specified radial functions, which result in significant improvements in the acceptance probability [59].

2.2. Setting up initial atomic structures

YSZ and GDC have the fluorite (CaF_2) crystal structure. Each unit cell contains four cations (Zr^{4+} or Y^{3+} in YSZ, Ce^{4+} or Gd^{3+} in GDC) forming a face-centered cubic (fcc) cation sublattice. The eight tetrahedral interstitial sites of the fcc unit cell are occupied by oxygen ions or oxygen vacancies forming a simple cubic anion sublattice.

A simulation cell contains two single crystals separated by two $\Sigma 5(310)/[001]$ pure tilt GBs (with tilt angle $\Theta = 36.9^\circ$) [63]. Periodic boundary conditions are applied in all three directions, resulting in an infinite array of planar GBs with $(12a/\cos\frac{\Theta}{2})$ spacing (where a is the lattice constant). The atomic structure is constructed in the following steps, where we explain the procedure using YSZ as an example.

1. Create two ZrO_2 perfect crystals with x , y and z axes along the [100], [010] and [001] crystal orientations, respectively.
2. Rotate the two crystals about the z axis by half the tilt angle in opposite directions. The x and y axes are now aligned with the $\langle 310 \rangle$ orientations.
3. From each crystal, cut out a rectangular cuboid that maintains structural periodicity in the x and y directions. The lengths of the rectangular cuboid in the x and y directions must be integer multiples of $3a/\cos\frac{\Theta}{2}$. The final size is set to $(6a/\cos\frac{\Theta}{2}) \times (6a/\cos\frac{\Theta}{2}) \times 6a$ in this study.
4. The two single crystals are joined together along the x axis to create a bicrystal with two $\Sigma 5(310)/[001]$ GBs per simulation cell under periodic boundary conditions. The final dimensions of the simulation cell are the same as those of the rectangular cuboids except the x length is doubled.
5. All ions are shifted in the x direction by a quarter length of the simulation cell for better visualization of the GBs. Now the GB planes do not coincide with the cell boundaries, and this enables easier analyses of the simulation results. After this, certain ions of the same sign get very

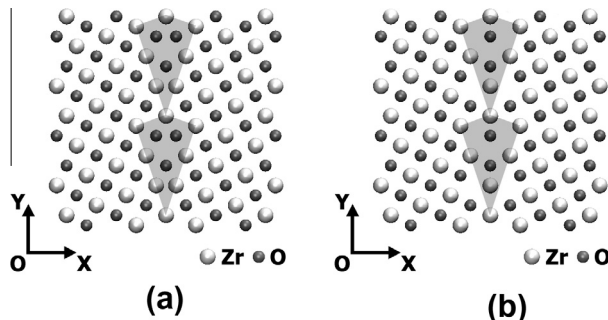


Fig. 1. The (a) unmodified and (b) modified interfacial structures of a ZrO_2 simulation cell with $\Sigma 5(3\bar{1}0)/[001]$ GBs. The shaded areas show the repeating unit of the GB.

- close to each other near the GBs, as shown in Fig. 1a. We refer to this as the unmodified structure, which is later found to be energetically unfavorable.
6. To improve structural stability, we remove one ion in each of these ionic pairs and shift the remaining one to the GB plane, as shown in Fig. 1b. The resulting structure is called the modified structure, which is confirmed to also be charge neutral.
 7. Create point defects according to the desired doping level by substituting Zr^{4+} ions with Y^{3+} ions and introducing oxygen vacancies by randomly removing one O^{2-} ion for every two Y^{3+} dopants. A YSZ simulation cell with the modified interfacial structure at this stage is shown in Fig. 2a.
 8. Relax the structure to a local energy minimum using the conjugate gradient relaxation method. Fig. 2b shows a system with the modified structure after this step. The interfacial region looks tightly bound, with no identifi-

able structural anomalies. On the other hand, systems with the unmodified structure display excessive amounts of free space and GB sliding (not presented here) after the initial relaxation.

9. Finally, simulation cells are equilibrated by MD simulations in the *NPT* ensemble for 200 ps using the Gear 6th-order predictor-corrector algorithm, with a time step of 0.5 fs. A Nose-Hoover thermostat [64–66] and the Parrinello-Rahman method [67] are employed to control the temperature at 2000 K and the pressure at the desired value. In this study, three different pressure conditions (0 and ± 3 GPa) are considered.

During the MD equilibration, simulation cells with the unmodified structure exhibit significant GB sliding (along the y and z axes), indicating that they are energetically unfavorable. Simulation cells with the modified structure, on the other hand, are quite stable. Hence we conclude the modified structure is a more realistic model of this specific type of GB. Dickey et al. [68] studied the atomic structures of the $\Sigma 5(3\bar{1}0)/[001]$ and $\Sigma 13(5\bar{1}0)/[001]$ tilt grain boundaries using Z-contrast scanning transmission electron microscopy (STEM), and their results are consistent with our modified structure. For the rest of the paper, we will focus on the modified structure.

During the equilibration MD simulations, we observe substantial diffusion of oxygen ions, but no cation moves away from its randomly chosen initial position. The lack of cation diffusion can be attributed to its high activation energy barrier, the absence of cation vacancies and the limited timescale of the MD simulations. Nonetheless, the resulting structures provide the initial conditions for the

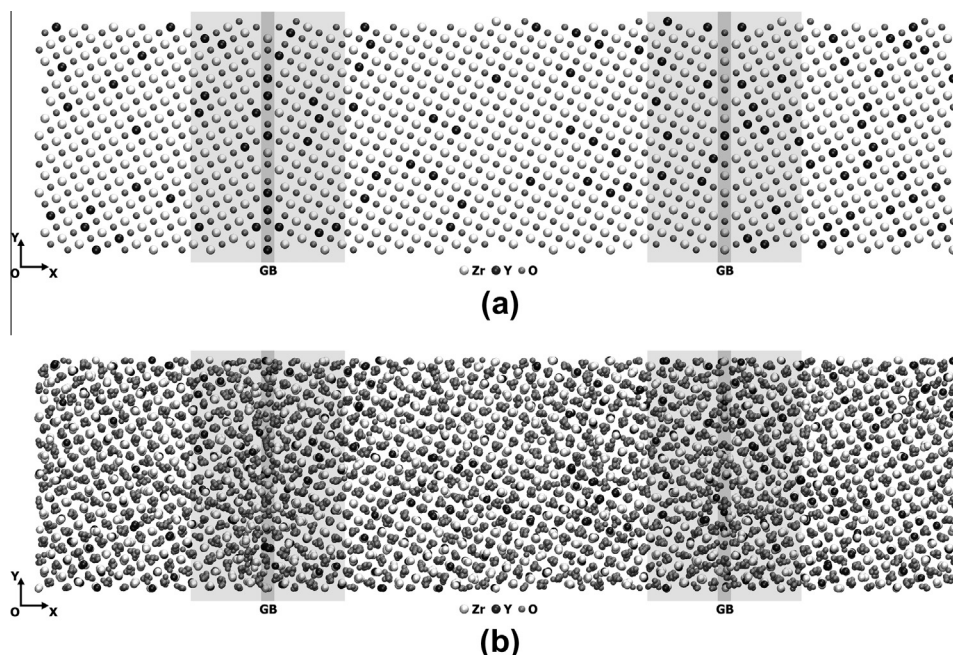


Fig. 2. Snapshots of a YSZ simulation cell with $\Sigma 5(3\bar{1}0)/[001]$ GBs, with the modified interfacial structure after (a) initial construction and (b) CG relaxation.

subsequent hybrid MC–MD simulations, which will equilibrate both cation and anion distributions.

2.3. Visualization

In this study, two methods are used to present the simulation results. First, since most of the available experimental results are in the form of simple one-dimensional (1-D) plots, we attempted to convert our simulation results to a similar form. To accomplish this, a 1-D Gaussian distribution function centered at its x coordinate is assigned to each ion in the simulation cell. These individual 1-D Gaussians are then superimposed to calculate the overall density distribution function. Hence the 1-D density distribution $\rho(x)$ to find a particle at position x can be given as

$$\rho(x) = \frac{1}{L_Y L_Z} \frac{1}{\sqrt{2\pi}\sigma} \sum_{i=1}^N \exp \left[-\frac{(x - x_i)^2}{2\sigma^2} \right] \quad (1)$$

where σ is the width of the 1-D Gaussian, N is the number of particles, x_i is the x -coordinate of particle i , and L_Y and L_Z represent the lengths of the simulation cells in the y and z directions, respectively. As expected, a wider Gaussian will reduce the spatial resolution of the density plots, whereas a narrower Gaussian will result in noisy profiles that can be difficult to interpret. In this study, the Gaussian width is empirically set to $\sigma = 0.9 \text{ \AA}$ so that the resulting plots will provide smooth distribution profiles.

In the second approach, 2-D density distributions are also computed by using a 2-D Gaussian function, the width of which is also empirically set to $\sigma = 0.9 \text{ \AA}$. The computed 2-D density maps resemble the images from high-resolution TEM. The 2-D density distribution $\rho(x, y)$ can be obtained as

$$\rho(x, y) = \frac{1}{L_Z} \frac{1}{2\pi\sigma^2} \sum_{i=1}^N \exp \left[-\frac{(x - x_i)^2}{2\sigma^2} - \frac{(y - y_i)^2}{2\sigma^2} \right] \quad (2)$$

where y_i is the y coordinate of particle i .

3. Results

Twelve YSZ and 12 GDC simulation cells with different initial defect distributions are prepared and then subjected to hybrid MC–MD simulations. Unless otherwise specified, the results presented below are averaged over the 12 systems for each condition. Each hybrid MC–MD simulation contains about 1×10^7 MC trial steps, which lead to approximately 3×10^4 – 6×10^4 successful “switch moves” at $T = 2000 \text{ K}$. A qualitative trend of energy reduction can be observed during the first 15,000–30,000 accepted MC moves, indicating that the systems are settling down toward the equilibrium states. Equilibrium elemental distributions are obtained by averaging over 1200 snapshots from the last periods of the 12 hybrid MC–MD simulations; 100 snapshots are taken from each simulation after 30,000 successful MC moves (one snapshot for every 100 accepted MC moves).

3.1. Dopant segregation

Let us first examine the dopant density distributions in 10 mol% YSZ and GDC with $\Sigma 5(310)/[001]$ GBs at $T = 2000 \text{ K}$ and zero pressure.

Fig. 3a shows the positions of Y^{3+} ions projected onto the x – y plane during the last 10,000 successful MC switch moves (superimposing 100 snapshots) of the hybrid MC–MD simulations, when the systems are assumed to have reached equilibrium. Despite their low concentration, Y^{3+} dopants seem to have visited almost all the cation sites, which implies that the dopant distributions are well equilibrated by the hybrid MC–MD simulations.

Fig. 3b–d shows the one-dimensional density distributions of Y^{3+} , Zr^{4+} and O^{2-} ions (as solid lines) along the x axis from the final results of the hybrid MC–MD simulations, respectively. The ionic density distributions at the beginning of the hybrid MC–MD simulations are also presented (as dashed lines) for comparison.

Fig. 3b clearly shows that Y^{3+} ions segregate to the GBs after reaching equilibrium, in contrast to the noisy profile of the initial density distribution (dashed line). The segregation occurs predominantly within about 1.5 nm from the GB core, which gives the segregated region a thickness of about 3.0 nm. Interestingly, there also is slight depletion near the GB cores, and these rapid fluctuations are likely caused by the unusual microstructure near the grain boundary plane.

Zr^{4+} and O^{2-} densities in **Fig. 3c** and d also show a few interesting features. The Zr^{4+} ions appear to have a quite smooth profile throughout the simulation cell, but substantial depletion is confirmed near the GBs. This is quite natural because, as the Y^{3+} dopants segregate to the GBs, the Zr^{4+} ions become more scarce. However, the sharp drop near the GB cores is present even before the hybrid MC–MD simulations. The details of the 1-D profiles near the GB planes reveal that the depletion becomes even more pronounced as a result of dopant segregation, though the magnitude of the depletion is not very sensitive to the dopant segregation. The near-GB depletion of host cations must be caused by the geometry of the GB structure, which can result in a local decrease in material density.

The O^{2-} density in **Fig. 3d** supports this hypothesis, since the profiles also show quite pronounced depletion near the GB cores. Unlike Zr^{4+} and Y^{3+} ions, O^{2-} density distributions look virtually unchanged in this plot, but this is an artifact of the scale of the plot. Enlarged views reveal noticeable variations in the GB region as a result of dopant segregation. Since Y^{3+} dopants and O^{2-} vacancies are of opposite charge, they should be drawn to each other through Coulombic attraction. Our results support this premise.

Fig. 4a shows the positions of Gd^{3+} ions projected onto the x – y plane during the last periods of the hybrid MC–MD simulations. Just like Y^{3+} ions in YSZ, Gd^{3+} dopants appear to have visited almost all the cation sites despite their low concentration.

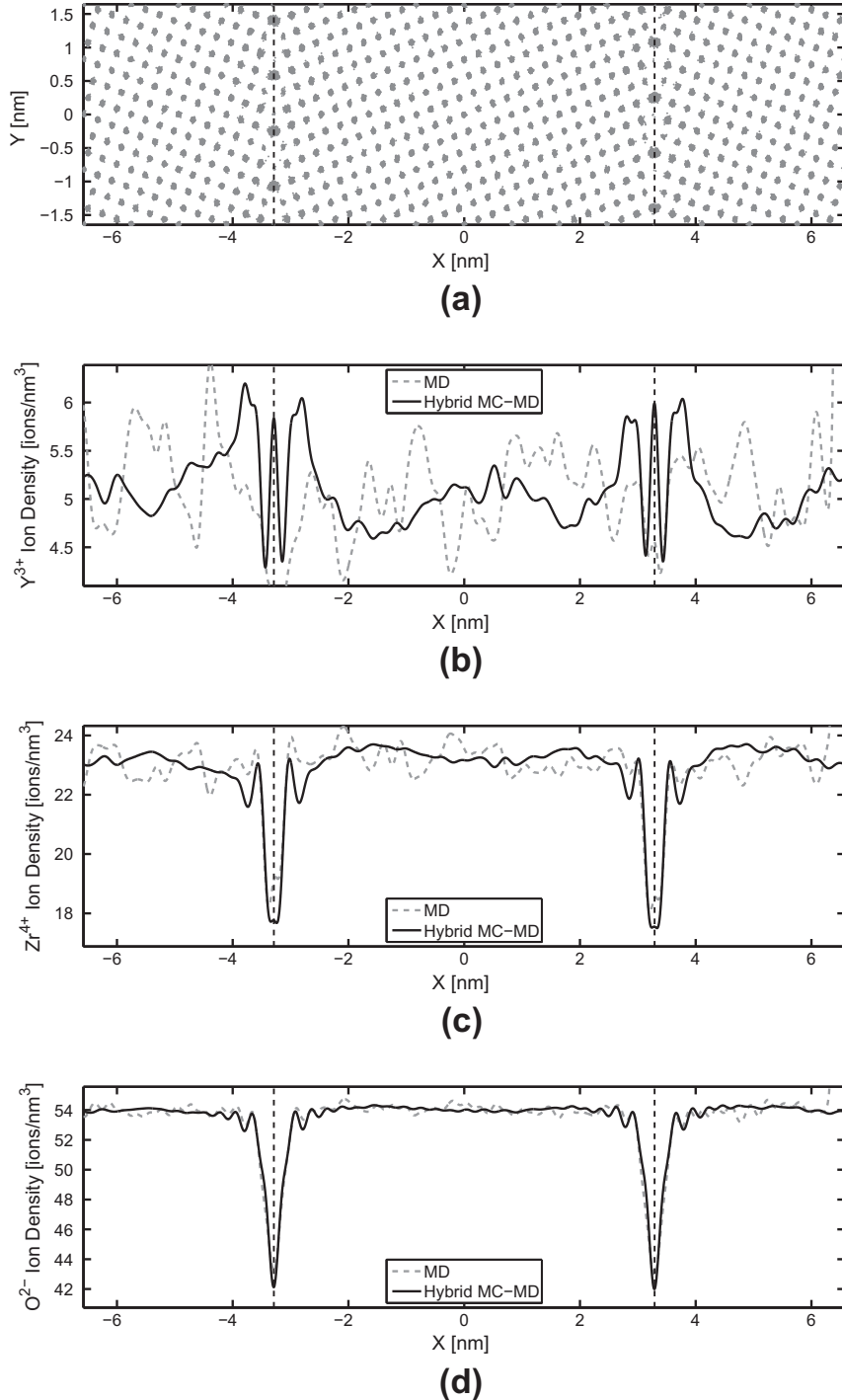


Fig. 3. (a) Dopant positions projected onto the x - y plane, (b) 1-D dopant density distributions, (c) 1-D host cation density distributions and (d) 1-D oxygen density distributions along the x axis in 10 mol% YSZ with $\Sigma 5(310)/[001]$ GBs at $T = 2000$ K and zero pressure. The solid lines represent the final results of the hybrid MC-MD simulations and the dashed lines represent the distributions before the hybrid MC-MD simulations.

Fig. 4b-d shows the 1-D density distributions of Gd^{3+} , Ce^{4+} and O^{2-} ions (as solid lines) along the x axis from the final results of the hybrid MC-MD simulations, respectively. The ionic density distributions at the beginning of the hybrid MC-MD simulations are also presented (as dashed lines) for comparison.

Fig. 4b shows pronounced segregation of Gd^{3+} ions to the GBs in the final periods of the hybrid MC-MD simu-

lations, in contrast to the noisy profile of the initial density distribution (dashed line, from the MD simulations). The Gd^{3+} dopants appear to be heavily concentrated within about 1.0 nm from the GB core, which establishes a segregation region that is about 2.0 nm thick. This appears to be slightly narrower than that of YSZ. Unlike YSZ, the segregation profile looks clear and straightforward, without any noticeable depletion.

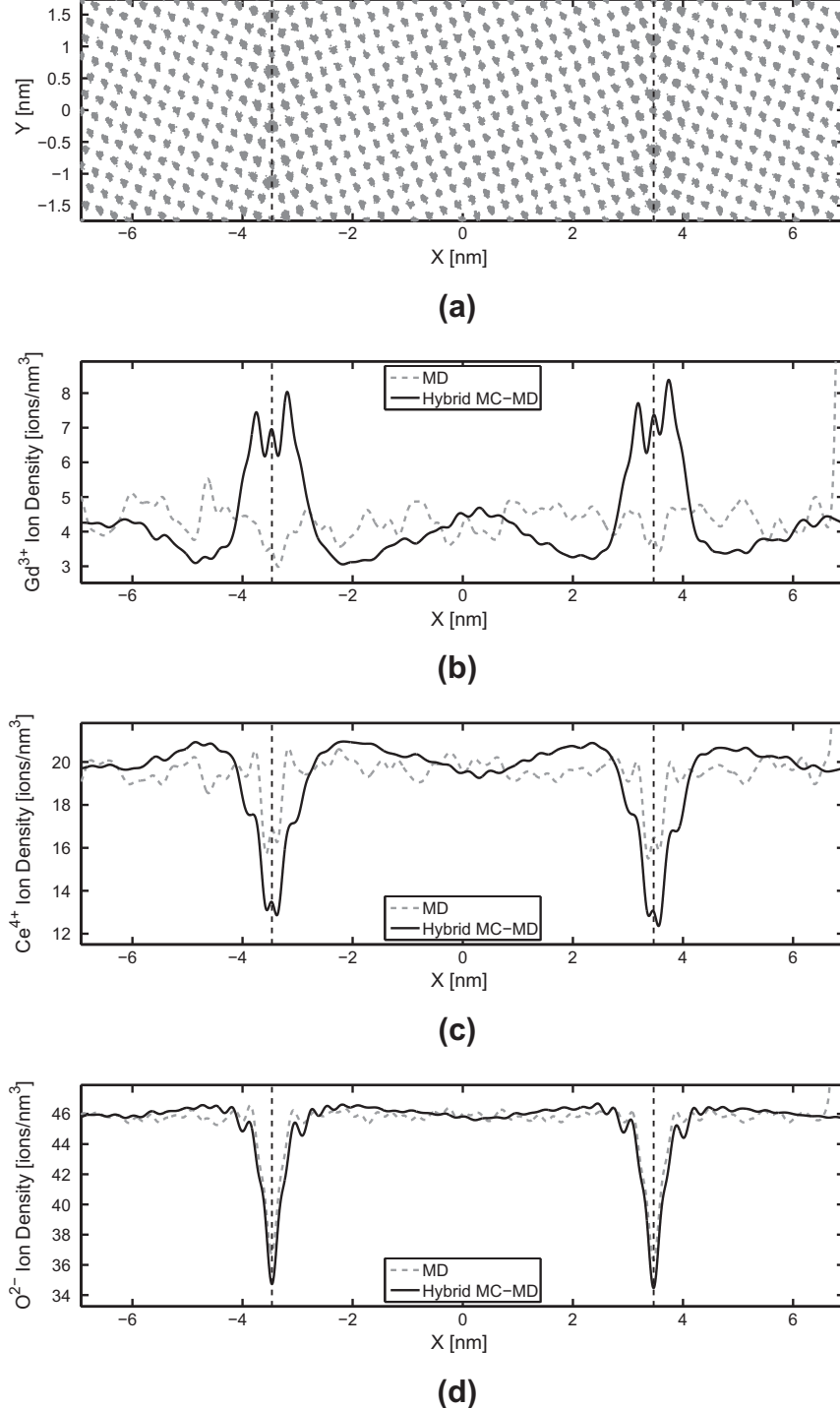


Fig. 4. (a) Dopant positions projected onto the x - y plane, (b) 1-D dopant density distributions, (c) 1-D host cation density distributions and (d) 1-D oxygen density distributions along the x axis in 10 mol% GDC with $\Sigma 5(310)/[001]$ GBs at $T = 2000$ K and zero pressure. The solid lines represent the final results of the hybrid MC-MD simulations and the dashed lines represent the distributions before the hybrid MC-MD simulations.

Fig. 4c and d shows Ce⁴⁺ and O²⁻ density distributions. The Ce⁴⁺ density distribution appears quite different from that of Zr⁴⁺ ions; the depletion near the GBs is much more pronounced due to heavier GB segregation of dopants during the hybrid MC-MD simulations.

The O²⁻ density in Fig. 3d also shows a significant difference (even in this scale of plot) before and after the hybrid MC-MD simulations. Depletion near the GBs is quite noticeable, which is consistent with the Coulomb attraction between Gd³⁺ dopants and oxygen vacancies.

3.2. Comparison between YSZ and GDC

Fig. 5a and b shows the ratios of dopant to host cation densities in YSZ and GDC, respectively. These normalized ratios are not affected by local variations in the material density, and therefore provide more accurate measures of the level of dopant segregation.

Comparison between the two parts of the figure clearly reveals that these two materials, though having identical crystal structure and GB type, exhibit completely different segregation behaviors. YSZ shows three pronounced segregation peaks (one main peak, along with two satellite peaks about 6 Å away) for each GB in a slightly broader (about 3.0 nm) segregation region. GDC, on the other hand, shows a single, much stronger segregation peak for each GB in a slightly narrower (about 2.0 nm) segregation region. GDC offers a much higher degree of segregation than YSZ despite the smaller ionic size mismatch between host and dopant cations, and this will be discussed in Section 4.

3.3. Comparison with experiments

In order to quantify the GB segregation and compare it with existing experiments, we define two 2 nm thick layers centered at the GB interfaces (lightly shaded areas in **Fig. 2**) as the GB region and the rest of the simulation cell as the bulk region, and compute the average dopant to host cation ratio in both regions. In YSZ, the averaged Y^{3+} to Zr^{4+} ratio is 0.250 in the GB region and 0.212 in the bulk

region. The ratio of these two numbers gives a segregation factor of 1.182.

The experimental measurements of segregation factor in YSZ under similar conditions are reproduced in **Table 1**. The experimental values fall in the range of 1.2–2.4, which is larger than the prediction from our simulations (1.182). This discrepancy may be attributable to the differences in the GB type and the temperature between the simulations and the experiments. It may also be caused by inaccuracies of the empirical interatomic potential models used in our simulations. The ratio of these two numbers gives a segregation factor of 1.846 for GDC. Since the dopant segregation is much more pronounced and the size of the simulation cell is limited, the equilibrium dopant concentration in the bulk drops well below the initial average value. This implies that the simulated profiles may correspond to an overall doping level lower than 10 mol% in experiments.

As shown in **Table 1**, the only available experimental measurement of GB segregation factor in GDC is 2.78, which is also larger than our prediction (1.846). Nonetheless, our simulations predict a larger segregation factor in GDC than in YSZ, which is consistent with experiments.

3.4. Oxygen vacancy distributions

In the GB systems, the greater structural complexity in the interfacial region leads to additional challenges in extracting the spatial distribution of oxygen vacancies. The algorithm we used to calculate the oxygen vacancy

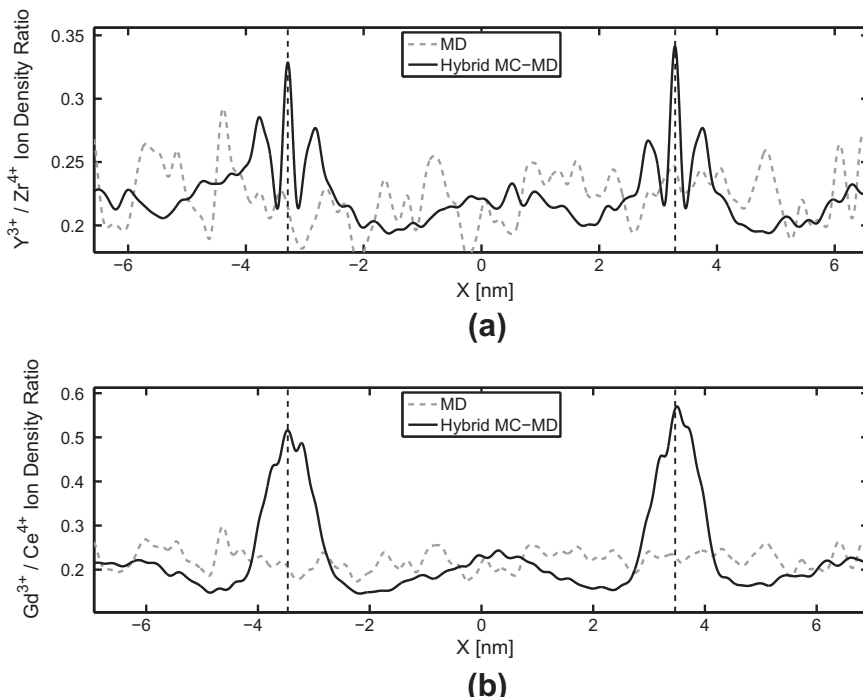


Fig. 5. The ratio of dopant to host cation 1-D densities along the x axis in 10 mol% (a) YSZ and (b) GDC with $\Sigma 5(310)/[001]$ GBs at $T = 2000$ K and zero pressure. Solid lines represent the final results of the hybrid MC–MD simulations and dashed lines represent the distributions before the hybrid MC–MD simulations.

Table 1

Experimental measurements of GB segregation in YSZ and GDC using such methods as X-ray photoelectron spectroscopy (XPS), Auger electron spectroscopy (AES), electron energy loss spectroscopy (EELS) and electron spectroscopy for chemical analysis (ESCA).

Material	Method (s)	Doping level (mol%)	T (K)	Y/Zr or Gd/Ce GB ratio	Seg. factor	Ref.
YSZ	AES	9.3	1456	0.325	1.503	[15]
	XPS	2.9	1923	0.111	1.568	[16]
	ESCA	2.0	1673	0.078	1.900	[17]
	XPS	5.0	1423	0.252	2.396	[18]
	XPS	5.0	1873	0.200	1.901	[18]
	AES/ESCA	6.0	1923	0.306	2.400	[19]
	EELS	2.9	1723	0.118	1.863	[23]
	EELS	3.0	1723	0.120	2.225	[23]
	EELS	10.0	Unspecified	0.500	2.000	[25]
	XPS	10.0	1873	0.283	1.274	[69]
GDC	EELS	11.1	Unspecified	0.695	2.780	[25]

distribution is explained in Appendix B. Fig. 6a and b shows the calculated oxygen vacancy density distributions in YSZ and GDC, respectively. The correlation between the dopant distribution (Fig. 5) and the vacancy distribution (Fig. 6) bears several similarities to our previous results on the (100) surface [59].

Let us first examine the oxygen vacancy distributions in both materials in the last period of the MD equilibration but before the hybrid MC–MD simulations, shown in Fig. 6a and b as dashed gray lines. In YSZ, the vacancy density on the GB interface (A) is lower than the bulk value, which indicates an excessive accumulation of oxygen ions. In GDC, the vacancy density at the core (A)

is slightly lower or similar to the bulk value. This is accompanied by two sharp peaks in the close vicinity (B), which represent the region where the oxygen ions on the GB interface come from, most likely as a result of near-GB vacancy formation. The GB results are analogous to the segregation of oxygen vacancies in the first anion layer beneath the (100) surface, contributing to an excess of oxygen ions on the surface, before dopant segregation in our previous study [59]. Hence oxygen vacancy segregation precedes dopant segregation. This can be attributed to the lower formation energy of oxygen vacancies near GBs. Oxygen vacancies are also depleted further away from the GB interface (C), which is a sign

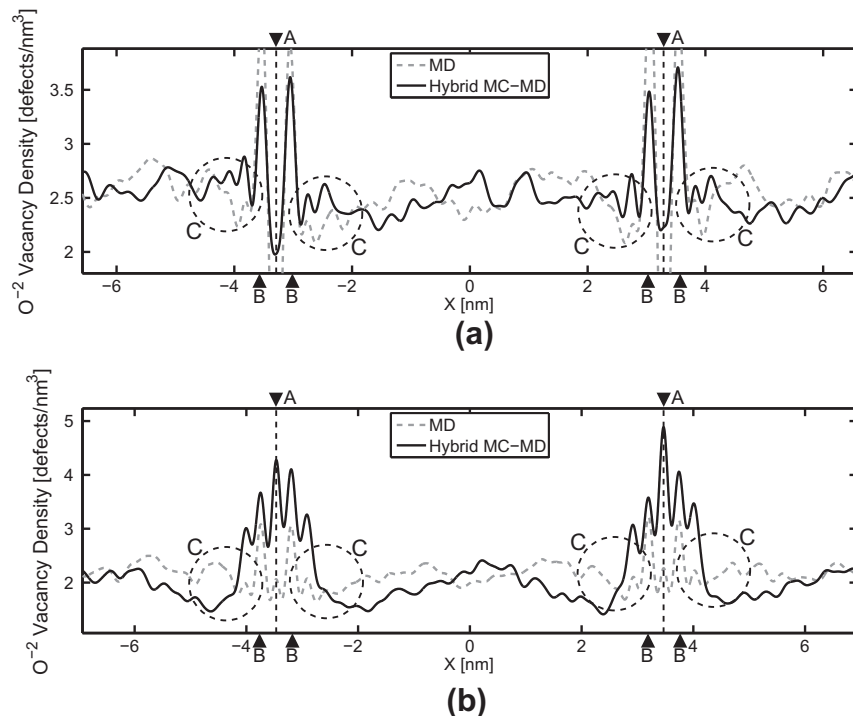


Fig. 6. 1-D oxygen vacancy density distributions along the x axis in 10 mol% (a) YSZ and (b) GDC with $\Sigma 5(310)/[001]$ GBs at $T = 2000$ K and zero pressure. Solid lines represent the final results of the hybrid MC–MD simulations and dashed lines represent the distributions before the hybrid MC–MD simulations.

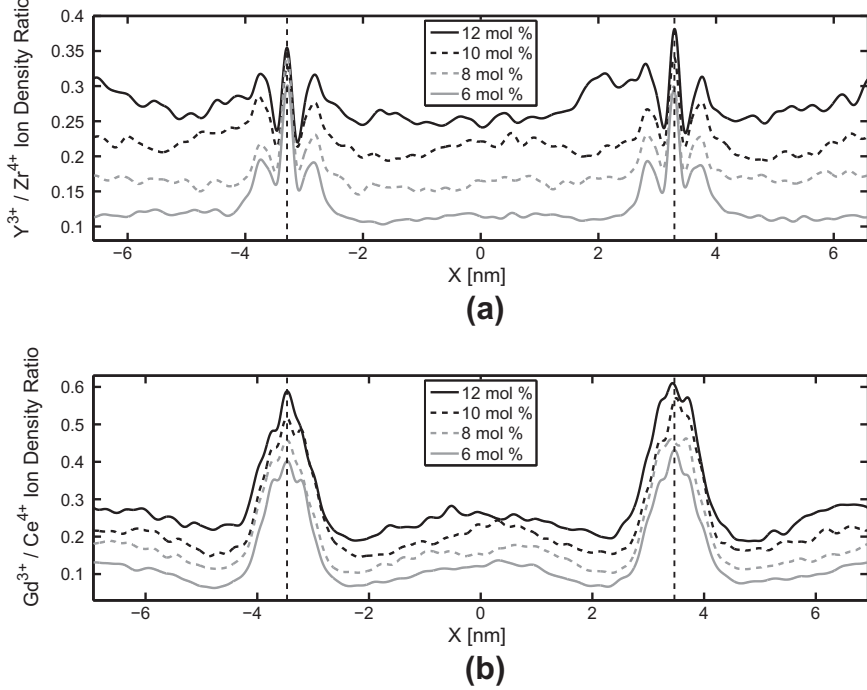


Fig. 7. 1-D dopant to host cation density ratio distributions along the x axis at four doping levels in (a) YSZ and (b) GDC with $\Sigma 5(310)/[001]$ GBs at $T = 2000$ K and zero pressure. All lines represent the final results of the hybrid MC–MD simulations.

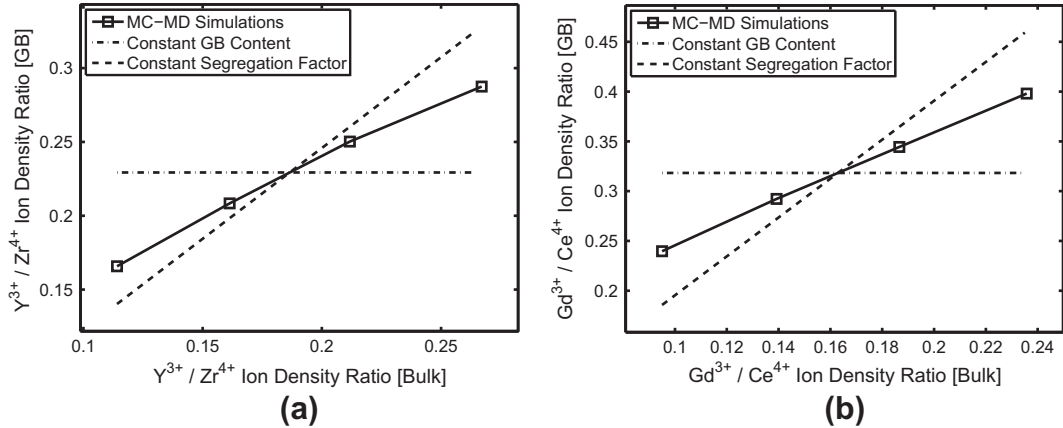


Fig. 8. Average ratio of dopant to host cation densities in the GB vs. that in the bulk at different doping levels in (a) YSZ and (b) GDC with $\Sigma 5(310)/[001]$ GBs at $T = 2000$ K and zero pressure.

of space charge layers that charge-compensate the vacancy-segregated GB interface.

After the dopant cations have also been equilibrated at the GBs, the extent of oxygen vacancy segregation at the GB cores is reduced in YSZ, whereas the opposite is true in GDC. At equilibrium, the dopant and vacancy distributions are positively correlated in GDC, whereas such a correlation is difficult to find in YSZ. Vacancy depletion in the space charge layers is diminished as a result of dopant segregation in both materials, although the extent of this transition is quite pronounced in GDC. In fact, GDC exhibits a higher degree of vacancy segregation as a consequence of dopant segregation, which is clearly not the case in YSZ. Similar trends were observed in our results on surface segregation [59] and can be attrib-

uted to the difference in defect ordering between these two materials.

Dopant cations in YSZ prefer oxygen vacancies as second nearest neighbors but not as first nearest neighbors. Hence dopant segregation reduces vacancy segregation (B) in YSZ, and vacancies are partially replenished in the space charge layers (C). In GDC, however, dopant cations prefer oxygen vacancies as both first and second nearest neighbors. Hence dopant segregation and vacancy segregation reinforce each other throughout the interfacial region in GDC. This also explains the higher segregation level in GDC than in YSZ despite the smaller size mismatch between dopant and host cations (in GDC than in YSZ).

Table 2

Dopant to host cation ratios in the GB and bulk regions and the corresponding segregation factor at four different doping levels ($\Sigma 5(310)/[001]$ GBs at $T = 2000$ K and zero pressure).

Material	Doping level (mol%)	Y/Zr or Gd/Ce GB ratio	Y/Zr or Gd/Ce bulk ratio	Segregation factor
YSZ	6.0	0.166	0.114	1.453
	8.0	0.208	0.161	1.292
	10.0	0.250	0.212	1.182
	12.0	0.287	0.267	1.077
GDC	6.0	0.240	0.095	2.522
	8.0	0.292	0.139	2.100
	10.0	0.344	0.187	1.846
	12.0	0.398	0.236	1.688

3.5. Doping level effects

Since the ionic conductivity of an ionic oxide is critically dependent on its doping level, it is of interest to examine how the segregation profiles are affected by the doping level of the material. Two scenarios have been proposed, based on the existing experiments on near-surface dopant segre-

gation. Some studies suggest that the interfacial concentration of dopants remains constant regardless of the doping level [70,71]. This translates to a decreasing segregation factor with a higher doping level. However, other studies claim that the GB segregation factor remains constant regardless of the overall doping concentration [69,72–74]. This means an increasing surface concentration of dopants with a higher doping level. Unfortunately, similar experimental data on GB segregation are not available yet.

Fig. 7a and b shows the predicted dopant to host cation ratio profiles for YSZ and GDC at four different doping levels. The shape of the segregation profile looks qualitatively the same for all four conditions (i.e. triple peaks in YSZ and a single peak in GDC).

The averaged dopant to host cation ratio in the GB region vs. that in the bulk region at the four doping levels is shown in Fig. 8a and b. On these plots, the scenario of constant dopant concentration at GB would correspond to a horizontal line (dashed-dotted line) and the scenario of constant segregation factor would correspond to a sloped line passing through the origin (dashed line).

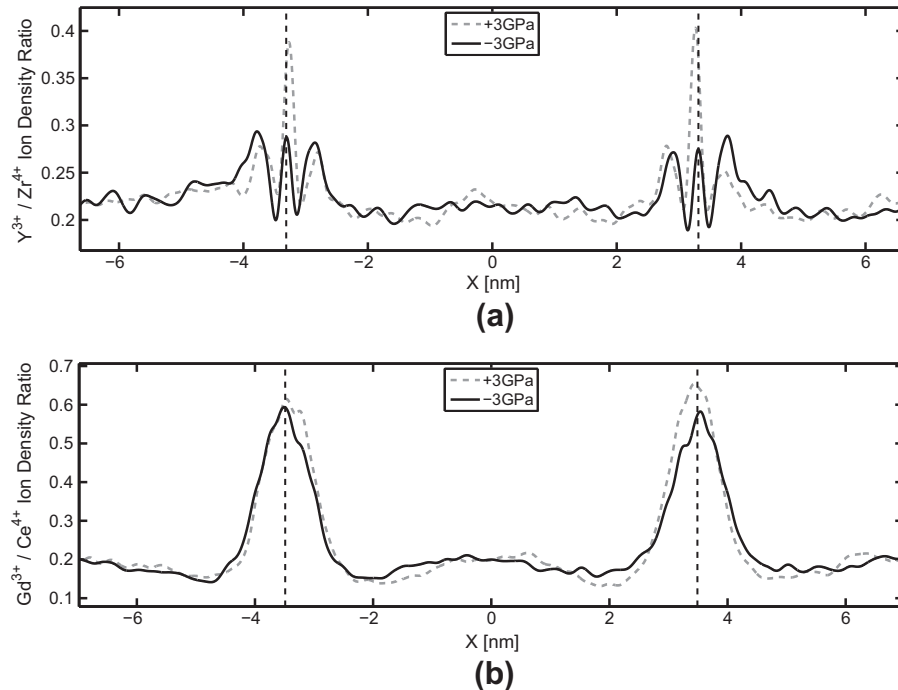


Fig. 9. 1-D dopant to host cation ratio at different pressures in 10 mol% (a) YSZ and (b) GDC with $\Sigma 5(310)/[001]$ GBs at $T = 2000$ K.

Table 3

Effects of pressure on the dopant to host cation ratios in the GB and bulk regions and the corresponding segregation factor. The results are for 10 mol% YSZ and GDC with $\Sigma 5(310)/[001]$ GBs at $T = 2000$ K and zero pressure.

Material	Doping level (mol%)	Y/Zr or Gd/Ce GB ratio	Y/Zr or Gd/Ce bulk ratio	Segregation factor
YSZ	+3 GPa	0.255	0.210	1.217
	-3 GPa	0.244	0.214	1.140
GDC	+3 GPa	0.351	0.184	1.907
	-3 GPa	0.338	0.189	1.790

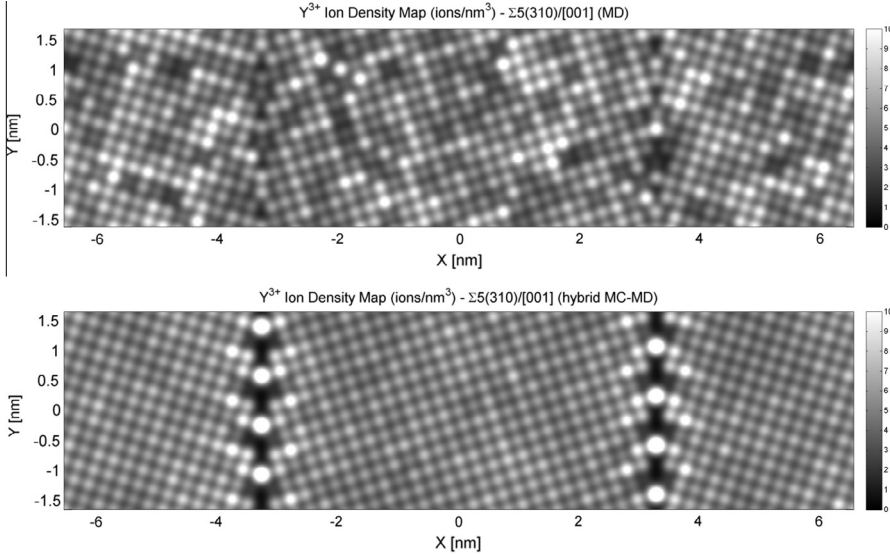


Fig. 10. 2-D Y^{3+} density distributions in YSZ from the last periods of the MD simulations (top) and the hybrid MC–MD simulations (bottom) with $\Sigma 5(310)/[001]$ GBs at $T = 2000$ K and zero pressure.

Fig. 8a and **b** shows that the predicted behavior in both YSZ and GDC is in between these two idealized scenarios. Of course, different results may be expected for different types of GBs other than the $\Sigma 5(310)/[001]$ type considered here. The results are summarized in **Table 2** in the form of average dopant to host cation ratios in the GB and bulk regions and the corresponding segregation factor.

3.6. Pressure effects

Lee et al. [57] showed that dopant segregation in metal oxides can exhibit a pressure dependence. In the case of Bi dopants in ZnO, hydrostatic pressure (compression) was shown to largely diminish interfacial segregation. Investigating the pressure dependence of dopant segrega-

tion in YSZ and GDC may offer a better understanding of the thermodynamics in these ionic oxides.

Fig. 9 shows the segregation profiles of dopants in YSZ and GDC under hydrostatic pressures of ± 3 GPa (the positive sign indicates hydrostatic compression and the negative sign indicates tension). The simulation results show that the pressure largely affects the height of the center peaks relative to the satellite peaks in YSZ. However, this level of detail would be hardly noticeable in experimental measurements due to their limited spatial resolutions. In GDC, the pressure effect on the segregation profile is also noticeable on the center peaks but is less pronounced.

To provide quantitative measures of the pressure effect, the average dopant to host cation ratios in the GB and bulk regions are listed in **Table 3**. In both materials, interfacial

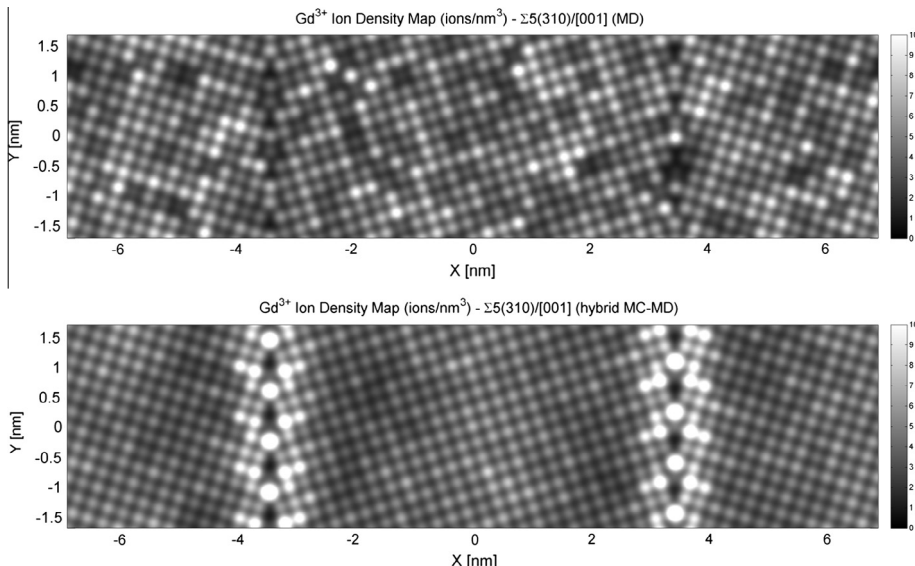


Fig. 11. 2-D Gd^{3+} density distributions in GDC from the last periods of the MD simulations (top) and the hybrid MC–MD simulations (bottom) with $\Sigma 5(310)/[001]$ GBs at $T = 2000$ K and zero pressure.

segregation is promoted by compression and suppressed by tension. The changes in the segregation profiles are of a moderate magnitude, even though 3 GPa is already much larger than the typical pressure that can be applied to solid electrolytes without causing mechanical failure. Nevertheless, it is interesting that these oxides respond to pressure in the opposite fashion compared to ZnO with Bi dopants [57].

3.7. 2-D elemental maps

In this section, some computation results will be presented in 2-D plots. In all figures, brighter tones correspond to higher ion densities and darker tones indicate the opposite.

Fig. 10 plots the 2-D Y^{3+} density distributions from the last periods of the MD (top) and the hybrid MC–MD (bottom) simulations. Unlike the random MD results (top), the hybrid MC–MD results (bottom), as already shown in the 1-D presentation (**Fig. 3b**), display obvious signs of GB segregation. Interestingly, there are also some locally depleted areas (dark patches) in the GB regions along with the distinct segregation peaks, and this pattern of segregation–depletion can be observed along the GBs with a strong periodicity. This type of detail was not observable in the 1-D presentation (**Fig. 3b**).

Fig. 11 plots the 2-D Gd^{3+} density distributions from the last periods of MD (top) and hybrid MC–MD (bottom) simulations. As in YSZ, the MD results (top) show a ran-

dom distribution, and no significant density change is observed throughout the simulation cell. On the other hand, the hybrid MC–MD results (bottom) show evident signs of GB segregation to a much higher degree than in YSZ. Like YSZ, GDC also displays pronounced structural patterns of dopant segregation, which were not observable in the 1-D presentation (**Fig. 4b**). There also are some locally depleted areas (small dark patches) in the GB regions, but these are of a much smaller size than in YSZ.

3.8. Segregation patterns

Figs. 12 and 13 present compilations of the 2-D elemental maps to summarize the results and help compare the distributions of different elements. All the results are from the hybrid MC–MD simulations, and the subplots show the enlarged elemental maps of a $2 \text{ nm} \times 2 \text{ nm}$ region near a $\Sigma 5(310)/[001]$ GB. The spatial range and density scale are kept the same for both materials for easier comparison.

In **Fig. 12**, Zr^{4+} (top left), Y^{3+} (top right), O^{2-} (bottom left) and cation (bottom right) densities are plotted to accentuate the differences between elements. In **Fig. 13**, Ce^{4+} (top left), Gd^{3+} (top right), O^{2-} (bottom left) and cation (bottom right) densities are also presented. YSZ shows a lesser degree of dopant segregation than GDC and more pronounced depletion areas in specific columns in the GB region. O^{2-} distributions in both materials generally offer lower densities near the GB cores, which correspond to local segregation of oxygen vacancies (GDC shows a

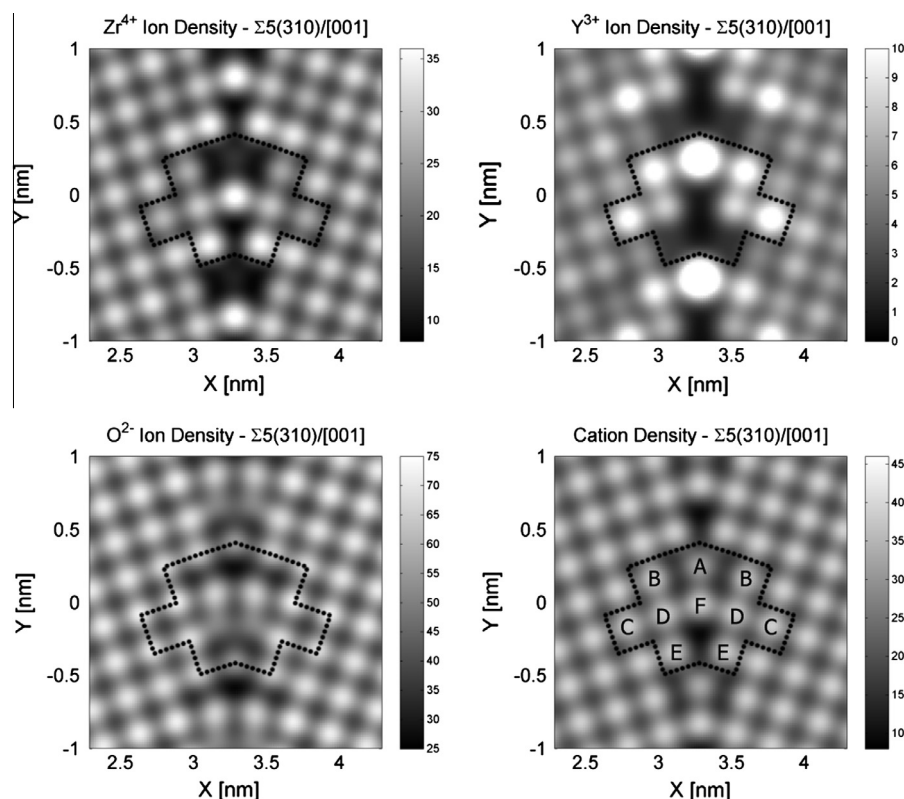


Fig. 12. Enlarged views of 2-D Zr^{4+} (top left), Y^{3+} (top right), O^{2-} (bottom left) and cation (bottom right) density distributions near a $\Sigma 5(310)/[001]$ GB in YSZ from the last periods of the hybrid MC–MD simulations at $T = 2000 \text{ K}$ and zero pressure.

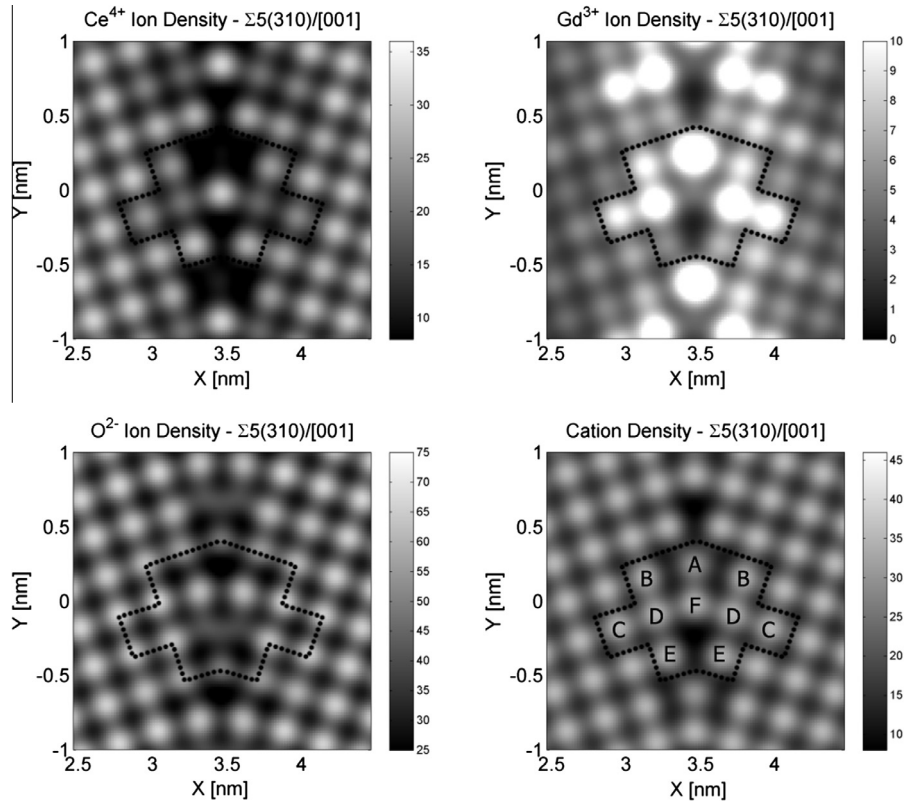


Fig. 13. Enlarged views of 2-D Ce^{4+} (top left), Gd^{3+} (top right), O^{2-} (bottom left) and cation (bottom right) density distributions near a $\Sigma 5(310)/[001]$ GB in GDC from the last periods of the hybrid MC–MD simulations at $T = 2000$ K and zero pressure.

higher degree of O^{2-} depletion due to a higher level of dopant and vacancy segregation). The cation densities present the details of the interfacial structure and suggests how high-resolution TEM images of this GB type may look.

4. Discussions

The 2-D profiles of GB segregation of YSZ and GDC raise a number of questions about the mechanism of dopant segregation. In our earlier study [59], based on the surface results, we concluded against the simple elasticity-based scenario that claims the size mismatch between the host and dopant cations is the dominant factor. In this scenario, the size misfit creates an elastic field and drives dopants to the interfacial region, where more free volume is available.

Recall that oxygen vacancy segregation precedes dopant segregation near the (100) surface and the $\Sigma 5(310)/[001]$ GB in both YSZ and GDC. In addition, GDC shows stronger dopant segregation than YSZ despite the smaller size mismatch between the host and dopant cations. Hence we again conclude that the dopant segregation is triggered by the vacancy segregation and largely controlled by the nature of dopant–vacancy association, which is a combination of short-range and long-range interactions. The GB segregation results in this work, however, reveal additional complexity through the column-by-column variations in the segregation profiles of these oxides.

One key finding from the last section is that the 2-D segregation profiles show a strong site dependence. Based on the segregation level, we categorize the interfacial columns into six different groups in Figs. 12 and 13. In YSZ, group A shows the strongest segregation, followed by groups B and C, which are quite similar to each other in the degree of segregation. The dopant density of group D is similar to or slightly above the bulk average. Groups E and F show dopant depletion, and group F has the lowest density of all. In GDC, group A still shows the strongest segregation. However, the second strongest segregation occurs at group D. This is the major difference between GDC and YSZ. Groups B and C also show segregation in GDC, similar to that in YSZ. Group E is similar to the bulk average, and group F is the only column in GDC that shows dopant depletion.

Both oxides display very strong site-by-site variations, but the differences in details make a noticeable distinction between the two. This is a clear indication that local chemistry plays an important role in interfacial segregation. If the segregation was mainly driven by the cation size mismatch, then we would expect groups E and F, which are adjacent to the free volume in the GB region, to exhibit the strongest segregation. However, in both YSZ and GDC, these two groups show the weakest segregation or even significant depletion of dopants. The simple elasticity-based scenario also fails to explain the much stronger segregation for group D in GDC compared to that in

YSZ. These observations give further support to our conclusion that elastic strain due to cation size mismatch is not the main driving force of the dopant segregation for the GB type examined in this study.

5. Summary

We performed hybrid MC–MD simulations to investigate the equilibrium distributions of point defects near the $\Sigma 5(3\ 1\ 0)/[0\ 0\ 1]$ GB in YSZ and GDC. The simulations confirmed segregation of both dopant cations and oxygen vacancies near the GBs in both materials. Vacancy segregation was shown to precede dopant segregation, and GDC exhibited a higher degree of dopant segregation than YSZ despite a smaller size mismatch between dopant and host cations. Our analysis also demonstrates the dependence of segregation behavior on the detailed geometry of the GB structure. Therefore we conclude that vacancy segregation and vacancy–dopant interaction are the dominant mechanisms of dopant segregation in these materials. The simple elasticity-based scenario based on the ionic size mismatch between dopant and host cations is not sufficient to explain the complex behavior of interfacial segregation. Dopant segregation was also affected by doping level and pressure, where the interfacial concentration of dopants was found to increase with both overall doping level and applied pressure.

Acknowledgements

This work is supported by a DOE/SciDAC Project on Quantum Simulation of Materials and Nanostructures and an NSF/DMR Grant No. 0907642.

Table A.4
BMB potential parameters for YSZ and GDC.

Interaction	A_{ij} (eV Å ⁶)	B_{ij} (eV)	C_{ij} (Å)	Reference
$\text{Y}^{3+}\text{O}^{2-}$	0.0	1345.1	0.3491	[60]
$\text{Zr}^{4+}\text{O}^{2-}$	0.0	985.869	0.376	[61]
$\text{O}^{2-}\text{O}^{2-}$	27.890	22764.300	0.149	[61]
$\text{Gd}^{3+}\text{O}^{2-}$	20.34	1885.75	0.3399	[51]
$\text{Ce}^{4+}\text{O}^{2-}$	20.40	1809.68	0.3547	[51]
$\text{O}^{2-}\text{O}^{2-}$	32.0	9547.96	0.2192	[51]

Appendix A. Interatomic potentials

The potential energy as a function of the ionic positions, \mathbf{r}_i ($i = 1, \dots, N$), can be written as

$$\begin{aligned} V(\{\mathbf{r}_i\}) &= V_{\text{BMB}}(\{\mathbf{r}_i\}) + V_{\text{Coulomb}}(\{\mathbf{r}_i\}) \\ &= \sum_{i=1}^{N-1} \sum_{j=i+1}^N \left[-\frac{A_{ij}}{|\mathbf{r}_{ij}|^6} + B_{ij} \exp(-C_{ij}|\mathbf{r}_{ij}|) \right] \\ &\quad + \sum_{i=1}^{N-1} \sum_{j=i+1}^N \frac{q_i q_j}{|\mathbf{r}_{ij}|} \end{aligned} \quad (\text{A.1})$$

where q_i is the effective charge of ion i and equals $+4e$, $+3e$ and $-2e$ for $\text{Zr}^{4+}/\text{Ce}^{4+}$, $\text{Y}^{3+}/\text{Gd}^{3+}$ and O^{2-} ions, respectively. $r_{ij} = |\mathbf{r}_j - \mathbf{r}_i|$ is the distance between ions i and j . The short-range potential parameters A_{ij} , B_{ij} and C_{ij} are taken from the literature [51,60,61], and they depend on the species of ions i and j (see Table A.4). The long-range Coulomb potential is computed by either the classical Ewald [75] or particle mesh Ewald [76,77] method in different parts of a simulation. All calculations are performed by MD++ (MD++ code is available at <http://micro.stanford.edu>).

Appendix B. Locating oxygen vacancies

In the fluoride structure, anions occupy a simple cubic sublattice and each anion has four nearest neighbor cations, as shown in Fig. B.14a. In the perfect ZrO_2 or CeO_2 crystal, four cations occupy corners of a cube. However, the presence of point defects distorts the cube into a six-faced polyhedron. If no oxygen ion resides inside, then the polyhedron contains a vacancy. Therefore, we can take the following steps to locate oxygen vacancies.

1. Partition the simulation cell into polyhedrons.
2. For each oxygen ion, determine which polyhedron it belongs in.
3. The number of vacancies in each polyhedron is $N_V = N_A - N_O$, where N_A is the number of anion sites originally assigned to the polyhedron, and N_O is the number of oxygen ions inside.

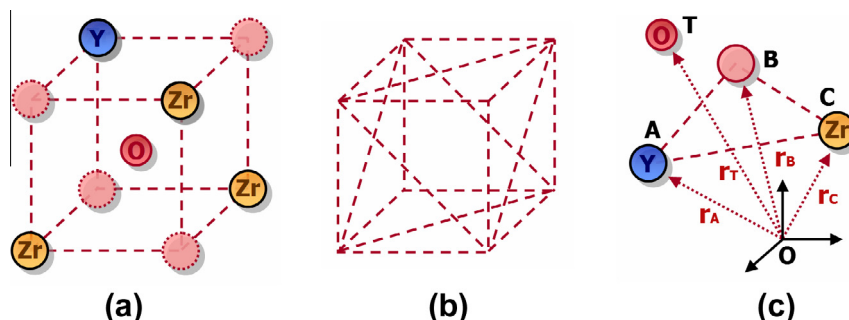


Fig. B.14. (a) A six-faced polyhedron defined by cation nodes. (b) Division of the faces. (c) Geometry of oxygen ion T relative to the triangle defined by three cation nodes A – B – C .

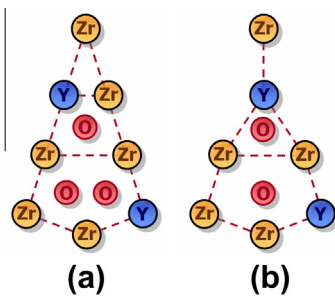


Fig. B.15. (a) An example of an interfacial partition for an unmodified YSZ GB structure. (b) An example of an interfacial partition for a modified YSZ GB structure.

Most of the polyhedrons will be six-faced, except those near GBs. The interfacial region needs to be treated separately, examples of which are given in Fig. B.15a and b. Some of these interfacial polyhedrons will have more than six faces.

As shown in Fig. B.14a, a typical six-faced polyhedron has eight corners (which will be called nodes), but only four of them are occupied by cations. Hence, to completely specify the polyhedron, we need to determine the coordinates of the other nodes. In this work, the positions of the non-occupied nodes are obtained by shifting the cation sublattice by half the lattice constant along the [001] direction. Because cations do not move significantly during the simulations, the initial partition of the simulation cell remains stable and unchanged.

To determine whether an oxygen ion, located at \mathbf{r}_T , is inside a polyhedron, we first divide the faces into a number of triangles, as shown in Fig. B.14b. For each triangle defined by \mathbf{r}_A , \mathbf{r}_B and \mathbf{r}_C , we compute the determinant of the following matrix:

$$M_{ABC} = \begin{vmatrix} x_A & y_A & z_A & 1 \\ x_B & y_B & z_B & 1 \\ x_C & y_C & z_C & 1 \\ x_T & y_T & z_T & 1 \end{vmatrix} \quad (\text{B.1})$$

where x_A, y_A and z_A are the coordinates of \mathbf{r}_A (and similarly for $\mathbf{r}_B, \mathbf{r}_C$ and \mathbf{r}_T). The nodes \mathbf{r}_A , \mathbf{r}_B and \mathbf{r}_C are ordered in such a way that the loop $\mathbf{r}_A-\mathbf{r}_B-\mathbf{r}_C$ and the outward normal of the polyhedron follow the right-handed rule. For an oxygen ion to exist inside the polyhedron, the determinants corresponding to all the above triangles that consist the polyhedron must have the same sign.

For a snapshot taken from a hybrid MC–MD simulation, the above procedure allows us to determine the “host” polyhedron for each oxygen ion. The number of oxygen ions N_O is then computed for each polyhedron, and the number of vacancies is simply $N_V = N_A - N_O(N_A$ is one for a conventional six-faced polyhedron, but could be different for the interfacial ones). Hence, in principle, N_V can be negative if $N_O > N_A$.

To construct the density plots in Fig. 6, we assign a 1-D Gaussian distribution function to each oxygen vacancy and

average over a number of snapshots as explained in Section 2.3.

References

- [1] Tschope A, Sommer E, Birringer R. Solid State Ionics 2001;139:255.
- [2] Zhou X-D, Huebner W, Kosacki I, Anderson HUJ. Am Ceram Soc 2002;85:1757.
- [3] Ruiz-Trejo E, Santoyo-Salazar J, Vilchis-Morales R, Benitez-Rico A, Gomez-Garcia F, Flores-Morales C, et al. Solid State Chem 2007;180:3093.
- [4] Boulfirad S, Djurado E, Dessemont L. Fuel Cells 2008;8:313.
- [5] Kosacki I, Suzuki T, Petrovsky V, Anderson HU. Solid State Ionics 2000;136:1225.
- [6] Suzuki T, Kosacki I, Anderson HUJ. Am Ceram Soc 2001;84:2007.
- [7] Suzuki T, Kosacki I, Anderson HU. Solid State Ionics 2002;151:111.
- [8] Suzuki T, Kosacki I, Anderson HUJ. Am Ceram Soc 2002;85:1492.
- [9] Knauth P. Solid State Ionics 2006;177:2495.
- [10] Knorer G, Reimann K, Rower R, Sodervall U, Schaefer H-E. PNAS 2003;100:3870.
- [11] Putkonen M, Sajavaara T, Niinisto J, Johansson LS, Niinisto LJ. Mater Chem 2002;12:442.
- [12] Shim JH, Chao C-C, Huang H, Prinz FB. Chem Mater 2007;19:3850.
- [13] Huang H, Shim JH, Chao C-C, Pornprasertsuk R, Sugawara M, Gur TM, et al. Electrochim Soc 2009;156:B392.
- [14] Nakagawa T, Sakaguchi I, Shibata N, Matsunaga K, Yamamoto T, Haneda H, et al. Mater Sci 2005;40:3185.
- [15] Winnubst AJA, Kroot PJM, Burggraaf AJJ. Phys Chem Solids 1983;44:955.
- [16] Nieh TG, Yaney DL, Wadsworth J. Scr Metall 1989;23:2007.
- [17] Hwang S-L, Chen I-WJ. Am Ceram Soc 1990;73:3269.
- [18] Boutz MMR, Winnubst AJA, Burggraaf AJJ. Eur Ceram Soc 1994;13:89.
- [19] Allemann JA, Michel B, Marki H-B, Gauckler LJ, Moser EMJ. Eur Ceram Soc 1995;15:951.
- [20] Aoki M, Chiang Y-M, Kosacki I, Lee J-R, Tuller H, Liu YJ. Am Ceram Soc 1996;79:1169.
- [21] Sakuma T, Ikuhara Y, Takigawa Y, Thavorniti P. Mater Sci Eng 1997;A234:226.
- [22] Ogawa H, Yasuda A, Shibata N, Ikuhara Y, Sakuma T. Philos Mag Lett 1998;77:199.
- [23] Stemmer S, Vleugels J, Van Der Biest OJ. Eur Ceram Soc 1998;18:156.
- [24] Shibata N, Oba F, Yamamoto T, Ikuhara Y, Sakuma T. Philos Mag Lett 2002;82:393.
- [25] Lei Y, Ito Y, Browning NDJ. Am Ceram Soc 2002;85:2359.
- [26] Shibata N, Oba F, Yamamoto T, Ikuhara Y. Philos Mag 2004;84:2381.
- [27] Matsui K, Ohmichi N, Ohgai M, Yoshida H, Ikuhara YJ. Ceram Soc Jpn 2006;114:230.
- [28] Guo X. Solid State Ionics 1995;81:235.
- [29] Guo X, Maier JJ. Electrochim Soc 2001;148:E121.
- [30] Guo X, Sigle W, Fleig J, Maier J. Solid State Ionics 2002;154–155:555.
- [31] Guo X, Zhang Z. Acta Mater 2003;51:2539.
- [32] Guo X, Ding YJ. Electrochim Soc 2004;151:J1.
- [33] Guo X, Waser R. Solid State Ionics 2004;173:63.
- [34] Guo X, Mi S, Waser RJ. Electrochim Soc 2005;8:J1.
- [35] Shimojo F, Okabe T, Tachibana F, Kobayashi M, Okazaki HJ. Phys Soc Jpn 1992;61:2848.
- [36] Shimojo F, Okazaki HJ. Phys Soc Jpn 1992;61:4106.
- [37] Okazaki H, Suzuki H, Ihata K. Phys Lett A 1994;188:291.
- [38] Okazaki H, Suzuki H, Ihata KJ. Phys Soc Jpn 1994;63:3556.
- [39] Li X, Hafskjold BJ. Phys: Condens Matter 1995;7:1255.
- [40] Brinkman HW, Briels WJ, Verweij H. Chem Phys Lett 1995;247:386.
- [41] Fisher CAJ, Matsubara H. Solid State Ionics 1998;113:311.
- [42] Khan MS, Islam MS, Bates DRJ. Mater Chem 1998;8:2299.

- [43] Fisher CAJ, Matsubara HJ. Eur Ceram Soc 1999;19:703.
- [44] Fisher CAJ, Matsubara H. Comput Mater Sci 1999;14:177.
- [45] Yamamura Y, Kawasaki S, Sakai H. Solid State Ionics 1999;126:181.
- [46] Zacate MO, Minervini L, Bradfield DJ, Grimes RW, Sickafus KE. Solid State Ionics 2000;128:243.
- [47] Schelling PK, Phillpot SR, Wolf DJ. Am Ceram Soc 2001;84:1609.
- [48] Pramananda Perumal T, Sridhar V, Murthy KPN, Easwarakumar KS, Ramasamy S. Physica A 2002;309:35.
- [49] Tang YW, Zhang Q, Chan K. Chem Phys Lett 2004;385:202.
- [50] Devanathan R, Thevuthasan S, Gale JD. Phys Chem Chem Phys 2009;11:5506.
- [51] Minervini L, Zacate MO, Grimes RW. Solid State Ionics 1999;116:339.
- [52] Inaba H, Sagawa R, Hayashi H, Kawamura K. Solid State Ionics 1999;122:95.
- [53] Hayashi H, Sagawa R, Inaba H, Kawamura K. Solid State Ionics 2000;131:281.
- [54] Hayashi H, Kanoh M, Quan CJ, Inaba H, Wang S, Dokuya M, et al. Solid State Ionics 2000;132:227.
- [55] Kim H-S, Kang E-TJ. Kor Ceram Soc 2001;38:698.
- [56] Mao Z, Sinnott SB, Dickey ECJ. Am Ceram Soc 2002;85:1594600.
- [57] Oyama T, Yoshiya M, Matsubara H, Matsunaga K. Phys Rev B 2005;71:224105.
- [58] Yoshiya M, Oyama TJ. Mater Sci 2011;46:4176.
- [59] Lee HB, Prinz FB, Cai W. Acta Mater 2010;58:2197.
- [60] Lewis GV, Catlow CRAJ. Phys C: Solid State Phys 1985;18:1149.
- [61] Dwivedi A, Cormack AN. Philos Mag A 1990;61:1.
- [62] Metropolis N, Rosenbluth AW, Rosenbluth MN, Teller AH, Teller E. J Chem Phys 1953;21(6):1087.
- [63] Bollmann B. Crystal defects and crystalline interfaces. Berlin: Springer-Verlag; 1970.
- [64] Nose S. Mol Phys 1984;52:255.
- [65] Nose SJ. Chem Phys 1984;81:511.
- [66] Hoover WG. Phys Rev A 1985;31:1695.
- [67] Parrinello M, Rahman AJ. Appl Phys 1981;52:7182.
- [68] Dickey EC, Fan X, Pennycook SJ. Am Ceram Soc 2001;84:1361.
- [69] Hughes AE, Sexton BAJ. Mater Sci 1989;24:1057.
- [70] Theunissen GSAM, Winnubst AJA, Burggraaf AJJ. Mater Sci Lett 1989;8:55.
- [71] Theunissen GSAM, Winnubst AJA, Burggraaf AJJ. Mater Sci 1992;27:5057.
- [72] Hughes AE, Badwal SPS. Solid State Ionics 1990;312–41.
- [73] Hughes AE. PhD dissertation, Royal Melbourne Institute of Technology, 1991.
- [74] Hughes AE, Badwal SPS. Solid State Ionics 1991;46:265.
- [75] DeLeeuw SW, Perram JW, Smith ER. Proc Roy Soc Lond Ser A 1980;373:27.
- [76] Darden T, York DM, Pedersen LGJ. Chem Phys 1993;98:10089.
- [77] Essmann U, Perera L, Berkowitz ML, Darden T, Lee H, Pedersen LGJ. Chem Phys 1995;103:8577.